Stable Targets for Spaceborne Microwave Radiometer Calibration

E. G. Njoku, S. K. Chan
Jet Propulsion Laboratory, California Institute of Technology
4800 Oak Grove Drive, Pasadena, CA 91109

R. L. Armstrong, M. J. Brodzik, M. H. Savoie, K. Knowles
CIRES/National Snow and Ice Data Center
University of Colorado, Boulder, CO 80309

Abstract-**Beginning in the 1970s, continuous observations of the Earth have been made by spaceborne microwave radiometers. Since these instruments have different observational characteristics, care must be taken in combining their data to form consistent long term records of brightness temperatures and derived geophysical quantities. To be useful for climate studies, data from different instruments must be calibrated relative to each other and to reference targets on the ground whose characteristics are stable and can be monitored continuously. Identifying such targets over land is not straightforward due to the heterogeneity and complexity of the land surface and cover. In this work, we provide an analysis of multi-sensor brightness temperature statistics over ocean, tropical forest, and ice sheet locations, spanning the period from 1978 to the present, and indicate the potential of these sites as continuous calibration monitoring targets.**

I. Introduction

The need to understand and monitor climate change has increased the importance of acquiring multi-decadal calibrated datasets of climate sensitive geophysical parameters. Over land, such data include observations of soil moisture, vegetation and snow cover that can be obtained globally using spaceborne microwave radiometers. Integrating these observations with modeling, in-situ, and other spaceborne data can provide useful insights into hydrologic cycle variability and change.

Conical-scanning microwave radiometers having similar but different observational characteristics have operated in space since the late 1970s, including the Nimbus-7 Scanning Multichannel Microwave Radiometer (SMMR), the series of DMSP Special Sensor Microwave/Imagers (SSM/I), the Tropical Rainfall Measuring Mission (TRMM) Microwave Imager (TMI), the ADEOS-II and EOS/Aqua Advanced Microwave Scanning Radiometer (AMSR and AMSR-E), and the Coriolis Windsat radiometer. These instruments were designed with built-in calibration systems to enable calibrated brightness temperatures to be derived from the sensor outputs in the ground processing. Fine-tuning of the calibration equations and coefficients is usually necessary for each sensor after launch due to the inability of pre-launch calibrations to fully characterize the instrument performance in orbit. The post-launch calibration corrections can remove residual artifacts in the processed data arising from errors in instrument pointing, component leakages, losses, and degradation, and unmodeled thermal gradients and system nonlinearities. The need for post-launch calibration correction is common to sensors across a wide spectral range, and a body of literature has developed for optical and infrared as well as for microwave calibration correction techniques [1]–[3].

A common method for post-launch radiometric calibration involves analysis of observations over homogeneous surface targets whose brightness temperatures are temporally stable and can be accurately modeled (for absolute calibration). Calm, cloud-free ocean regions have been used as reference targets at the cold end (~80-180 K) of the Earth-view brightness temperature range since their characteristics are relatively stable and the ocean/atmosphere column can be quite accurately modeled and measured at point locations using in-situ sensors [4], [5]. Antarctic ice sheets have been considered for calibration in the mid brightness temperature range (~150-250 K) [6], and tropical forests for calibration at the high end of the range (~250-300 K) [7], [8]. The inaccessibility of ice sheet and tropical forest regions, however, and their heterogeneity and structural complexity, have limited their characterization to date either by in-situ measurement or modeling. More study is needed to improve the potential of these sites as calibration targets.

In this paper we have investigated the multi-year brightness temperature variability of selected ocean, ice-sheet, and tropical forest sites as observed by the SMMR, SSM/I, and AMSR-E sensors, in order to identify and characterize optimum target areas for long-term radiometric calibration. A long-term objective is to develop procedures for calibration of spaceborne radiometer observations in a consistent manner across several satellite instruments. Data sets calibrated using such procedures may be used for generating climatological records of derived geophysical quantities. We have focused on data from the SMMR, SSM/I, and AMSR-E since these sensors span a multi-decadal period from 1978 to the present. The sensors are conically scanning with similar observational

TABLE I
INSTRUMENT CHARACTERISTICS

	SMMR (Nimbus-7)	SSM/I (DMSP-F08)	SSM/I (DMSP-F11)	SSM/I (DMSP-F13)	AMSR-E (Eos Aqua)
Center freq. (GHz)	6.6, 10.7, 18.0, 21.0, 37.0	19.35, 22.235(V), 37.0, 85.5	19.35, 22.235(V), 37.0, 85.5	19.35, 22.235(V), 37.0, 85.5	6.9, 10.7, 18.7, 23.8, 36.5, 89.0
Inc. Angle (deg)	50.3	53.1	53.1	53.1	54.8
3-dB footprint at 37 GHz (km)	27x18	37x29	37x29	37x29	14x8
Altitude (km)	955	832-851	841-878	844-856	705
Swath width (km)	780	1400	1400	1400	1445
Orbit; asc. node crossing	Polar, sun-sync; 12:00 noon	Polar, sun-sync; 6:15 am	Polar, sun-sync; 6:11 pm	Polar, sun-sync; 5:42 pm	Polar, sun-sync; 1:30pm
EASE-Grid Data period	Oct. 1978 - Aug. 1987	Jul. 1987 - Dec. 1991	Dec. 1991 - May 1995	May 1995 - present	May 2002 - present

characteristics, although the SSM/I does not have the two lower frequencies of the SMMR and AMSR-E (Table I).

II. INSTRUMENTS AND DATA

The characteristics of the instruments are listed in Table I, indicating their frequencies, incidence angles, spatial resolutions, swath coverage, and nodal crossings. The periods for which processed Equal-Area Scalable Earth-Grid (EASE-Grid) data are available for these sensors from the National Snow and Ice Data Center (NSIDC) are also indicated. The SMMR operated on the Nimbus-7 platform from October 1978 to August 1987. The swath data were reprocessed to correct for calibration anomalies [9], and interpolated to the 25 km EASE-Grid using an inverse-distance-squared method in which the weighted average was computed of brightness temperatures from samples within 25 km of the EASE-Grid cell center [10]. This method results in minimal smoothing while adding as little noise as possible.

The SSM/I has operated on various DMSP platforms since 1987. Table I lists the characteristics of SSM/I data from three of these platforms (F08, F11 and F13). Quality-controlled SSM/I brightness temperature swath data [11] were processed to correct for known geolocation and calibration anomalies. The swath data were interpolated to the 25 km EASE-Grid by employing a Backus-Gilbert optimum interpolation method, using the actual SSM/I antenna pattern to maximize the radiometric integrity of the original brightness temperatures [12]. The Backus-Gilbert method can be tuned to enhance resolution or reduce noise, but cannot achieve both simultaneously. The SSM/I EASE-Grid processing minimizes noise for all channels by interpolating to the lowest-resolution effective 3-dB footprint of the 19 GHz V-polarized channel.

The AMSR-E has operated on the Earth Observing System (EOS) Aqua platform since May 2002. AMSR-E Level 2A (Version 001) brightness temperature swath data were resampled for spatial consistency to a number of different resolutions [13]. The data were interpolated to the 25 km EASE-Grid using an inverse-distance-squared method.

All EASE-Grid daily brightness temperature data for the SMMR, SSM/I, and AMSR-E were gridded separately for ascending and descending passes.

III. ANALYSIS

To illustrate the temporal characteristics and stability of the SMMR, SSM/I and AMSR-E brightness temperatures, data were extracted at selected EASE-Grid point locations representative of three surface types: *ocean* (Indian Ocean, 34.9°S, 90.0°E); *ice sheet* (Dome 'C', Antarctica, 74.6°S, 123.0°E); and *tropical forest* (Salonga, Zaire, 1.5°S, 21.6°E). Fig. 1(a) shows the 10.7 GHz vertical polarization (10V) data from the SMMR and AMSR-E 'cold' passes. 'Cold' passes are those whose Equator crossings occur between approximately midnight and 6:15 am. Fig. 1(b) shows similar plots for the 37 GHz vertical polarization (37V) data from the SMMR, SSM/Is, and AMSR-E (actually 36.5 GHz for AMSR-E).

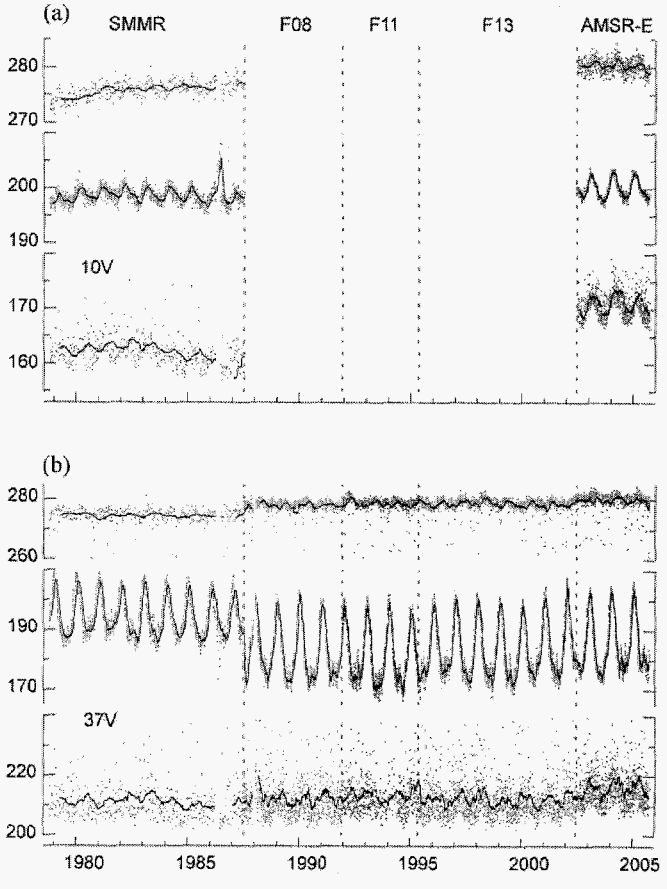

Fig. 1. Brightness temperature (*Tb*) time series for 'cold' passes of SMMR, SSM/I (F08, F11, F13) and AMSR-E. (a) 10GHz vertical polarization, (b) 37 GHz vertical polarization. *Upper trace*: Forest. *Middle trace*: Ice sheet. *Lower trace*: Ocean. The vertical axis *Tb* units are in Kelvins and the scales are different for (a) and (b).

The F13 SSM/I data are shown only up to the start of the AMSR-E time series. At 37V the ocean and forest data are quite consistent between SSM/I sensors, showing a small brightness temperature (*Tb*) annual cycle, with fairly uniform mean levels. The SMMR *Tb* levels are slightly lower, and the AMSR-E levels slightly higher, than the SSM/I over both ocean and forest. Over the ice sheet the SMMR data show a higher mean level and much smaller annual amplitude than the SSM/I and AMSR-E data. Similar observations can be made for the 10V data; however, the offsets between the SMMR and AMSR-E data are larger at the ocean and forest locations, and smaller at the ice sheet location, than for 37V. The spike occurring in the SMMR data in early-to-mid 1986 is due to a change in the instrument operating mode [9]. SMMR data after April 3, 1986 should be considered unreliable due to this factor and the subsequent platform and instrument degradation.

The sizes of the offsets observed in Fig. 1 indicate significant calibration level differences between the SMMR and other sensor data, while the SSM/I and AMSR-E data appear similar in calibration levels. Examination of data from all channels, and radiative transfer modeling, are necessary to determine how much of the differences observed in Fig. 1 are explainable by differences in sensor frequencies, incidence angles, and diurnal sampling times. The data traces shown in Fig. 1 indicate the potential of these surface types as calibration targets but also the limitation of considering single point locations as such targets. In the next sections of this paper we examine more spatially extensive or diverse as well as temporal characteristics of the target brightness temperatures. However, we leave descriptions of procedures for actual inter-sensor calibration adjustments to a subsequent study.

The challenge for post-launch radiometric calibration adjustment is to find observational targets of adequate spatial homogeneity and temporal stability. The targets should be homogenous over large enough areas to minimize nonlinear brightness temperature averaging and antenna pattern effects, while remaining stable and estimable in their brightness temperature characteristics. In this paper, we have examined regions of the global ocean, Antarctic ice sheet, and African tropical forest.

A. Ocean

In [4] and [5] methods were described for using ocean regions as brightness temperature calibration references. In [5], a histogram technique was used to identify brightness temperature minima, sensitive enough to detect calibration drifts of a few tenths of Kelvin per year. Here, we have investigated another approach using global ocean averages. In this method, six-day composite global brightness temperature (*Tb*) maps, for ascending and descending passes, are created from daily EASE-Grid data. A six-day period is necessary to obtain global coverage for the SMMR with minimal swath gaps. A moving window is used to create the six-day composite maps at a daily time step. Each six-day map is then averaged over a defined 'open ocean' area to obtain an ocean-average *Tb* value at a daily time step for each channel. The open ocean region is defined by excluding all land areas, all coastal ocean within five grid cells (~125 km) of land, and all regions poleward (north and south) of 44° latitude. This masking minimizes *Tb* contamination by land emission in the antenna sidelobes and sea ice at all seasons in the polar regions. Outliers are screened by using the middle 95th percentile of *Tb* values over the data period at each grid point. No dynamic screening is done for precipitation, clouds, or high winds.

Figs. 2(a) and 2(b) show the resulting ocean-average *Tb* time series for SMMR and AMSR-E descending pass data for the 6V, 6H, 37/36V, and 37/36H channels. The plots show the deviations from the mean for each channel over the displayed data time periods. The means and standard deviations for all channels are listed in Table II. The ocean-average *Tb* is thus found to be quite stable for both SMMR and AMSR-E with only a very small discernible annual cycle. The SMMR *Tb* level indicates a decrease, visible in the V-channels, occurring around day 1890 after launch.

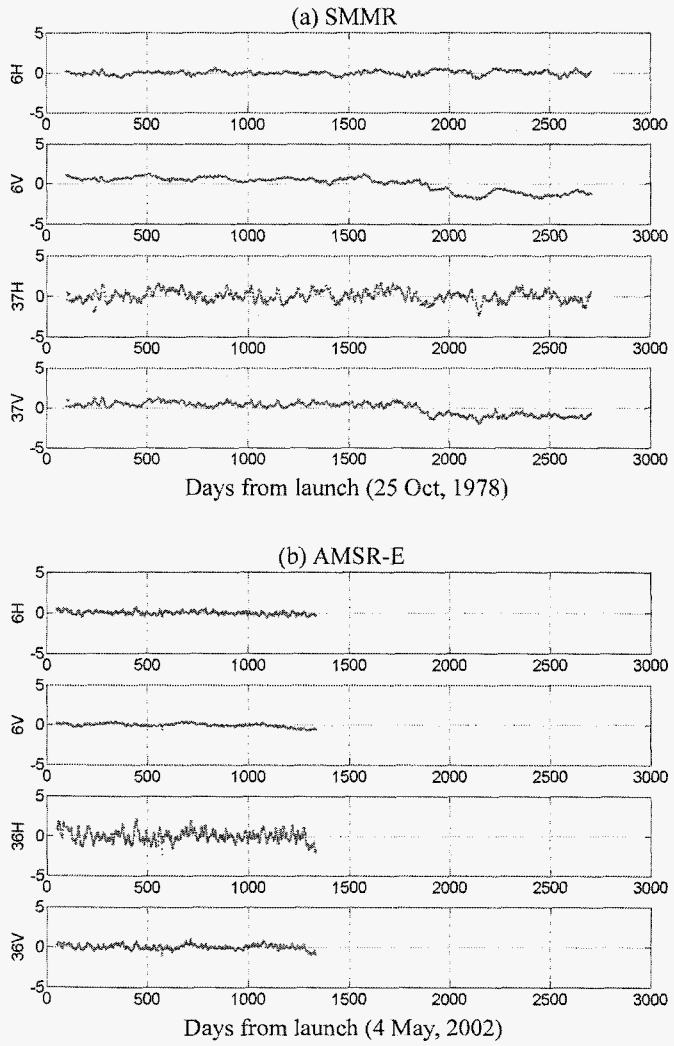

Fig. 2. Ocean-average brightness temperature (K) deviations from the long-term mean of the lowest and highest frequency channels, descending passes, of: (a) SMMR, and (b) AMSR-E.

TABLE II
MEANS (m) AND STANDARD DEVIATIONS (σ) FOR SMMR AND AMSR-E OCEAN-AVERAGE TIME SERIES.

	SMMR		AMSR	
Channel	m (K)	σ(K)	m (K)	σ(K)
6H	87.7	0.26	84.5	0.23
6V	158.1	0.87	170.6	0.22
10H	97.6	0.38	91.0	0.33
10V	167.1	0.73	175.8	0.20
18/19H	125.1	0.67	132.8	0.62
18/19V	187.6	0.61	201.8	0.36
36/37H	161.6	0.66	163.4	0.70
36/37V	216.6	0.74	223.1	0.30

This decrease appears linked to a step change in spacecraft attitude that occurred during the first week of January 1984, which caused a small and variable shift in incidence angle across the swath [9]. SMMR calibration anomalies also occurred during the first few months of the mission, and after April 3, 1986 during the "special operations" period, after which the instrument performance degraded [9]. Only data from 30 January, 1979 through 22 March, 1986 (days 97 through 2705) are shown in Fig. 2 for the SMMR. Fig. 2 indicates that the ocean-average *Tb* values are much more stable in time than the single-point ocean values (Fig. 1). Local seasonal and interannual cycles such as El Nino and ocean-current features are averaged out at the global scale. Hence, calibration drifts of a few tenths Kelvin can be readily detected using the ocean-averaging method.

B. Tropical Forest

A statistical procedure was used to examine the spatial homogeneity and temporal stability of brightness temperatures over tropical forest and ice sheet regions. For tropical forest, a region in central Africa was selected for study, consisting of a 100 x 100 array of 25-km EASE-Grid cells centered at 1.5°S, 21.6°E in the Salonga National Park, Zaire. We define a hypothetical satellite sensor 'footprint' as a set of 3 x 3 grid cells (approximately 75 km x 75 km) for a given day, centered at a particular grid point. The footprint is thus described by an array of N = 9 grid cells with indices j. The spatial mean and standard deviation of the observed brightness temperatures within the footprint on day i are:

$$m_i = \frac{1}{N}\sum_{j=1}^{N} Tb_{ij} \;; \quad \sigma_i = \sqrt{\frac{1}{N+1}\sum_{j=1}^{N}(Tb_{ij} - m_i)^2} \qquad (1)$$

At any grid point we can examine the time series of m_i and σ_i computed daily. These are shown in Fig. 3 for AMSR-E data during the year 2003 at the location of Salonga. Only the 10.6 GHz and 36.5 GHz, vertical polarization, descending pass data are shown.

The footprint means, m_i, show little seasonal variation in either the 10V or 37V channels, though the values are slightly higher, and with more scatter, in the first half of the year. The footprint standard deviations, σ_i, are quite uniform throughout the year.

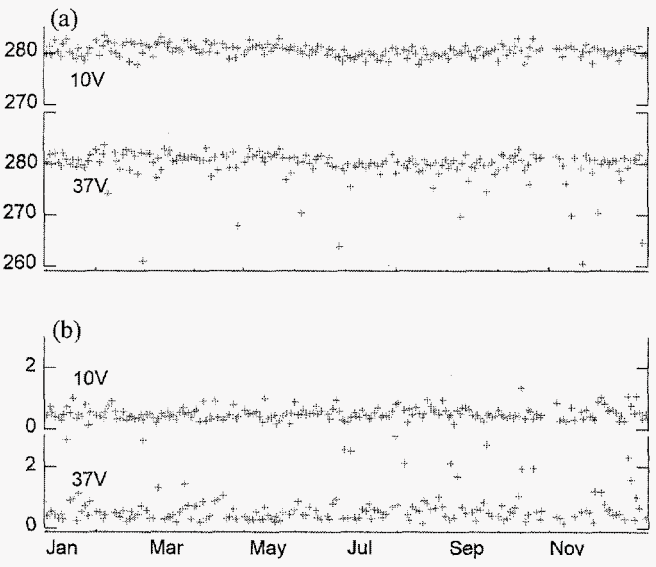

Fig. 3. Time series of AMSR-E *Tb* descending pass statistics for the year 2003 at Salonga, Zaire, for 10 GHz and 37 GHz vertical polarizations: (a) Footprint mean, m_i; (b) Footprint standard deviation, σ_i. Units are in Kelvins.

The temporal averages of m_i and σ_i computed over the year are:

$$\overline{m} = \frac{1}{N_D}\sum_{i=1}^{N_D} m_i \;; \quad \overline{\sigma} = \frac{1}{N_D}\sum_{i=1}^{N_D}\sigma_i \qquad (2)$$

where the overbar denotes the time-average and N_D is the number of available daily sampling points in a year. Thus, $\overline{m}$ represents the annual average of the footprint *Tb* mean, while $\overline{\sigma}$ represents the annual average of the footprint *Tb* standard deviation. *A low value of $\overline{\sigma}$ indicates that the footprint is spatially homogeneous and the homogeneity persists over a long time period such as a year.*

We can also compute:

$$\sigma_m = \sqrt{\frac{1}{N_D+1}\sum_{i=1}^{N_D}(m_i - \overline{m})^2} \qquad (3)$$

which represents the temporal standard deviation, taken over a year, of the footprint *Tb* mean. *A low value of σ_m indicates that the footprint Tb mean is temporally stable, with low seasonal variability.*

Taken together, images of $\overline{\sigma}$ and σ_m can be examined to identify areas with low values of these quantities, indicating a combination of footprint spatial homogeneity and low temporal variability. Such areas may be useful as calibration targets.

Fig. 4(a) shows an image of $\overline{m}$ for the AMSR-E 10 GHz vertical polarization for the year 2003. It indicates areas of low brightness over lakes and rivers, and high brightness over densely forested areas. The white cross (denoted 'Salonga' in this paper) is centered in a densely forested area. The images

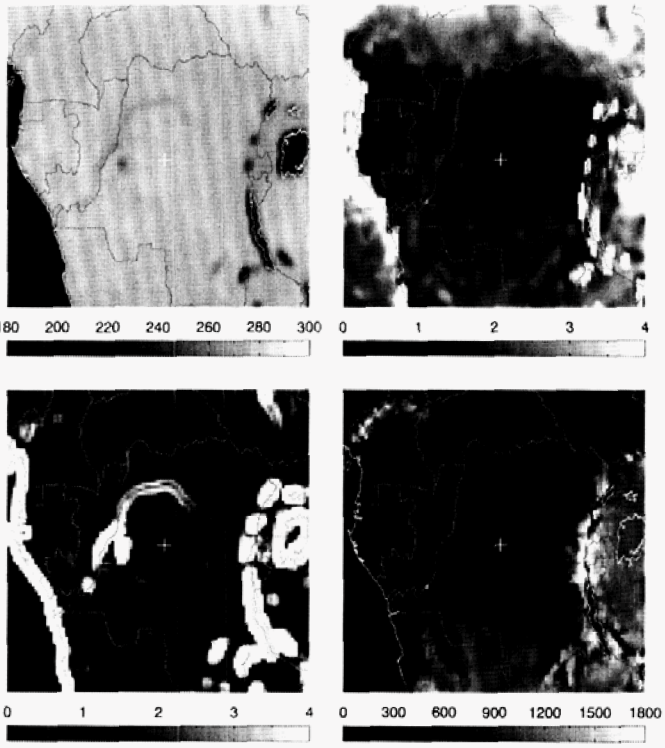

Fig. 4. Images of AMSR-E 10 GHz vertical polarization *Tb* statistics for central African tropical forest, descending passes, in 2003. (a) *Upper left:* $\overline{m}$ (K). (b) *Upper right:* σ_m (K). (c) *Lower left:* $\overline{\sigma}$ (K). (d) *Lower right:* Surface topography (meters above sea level).

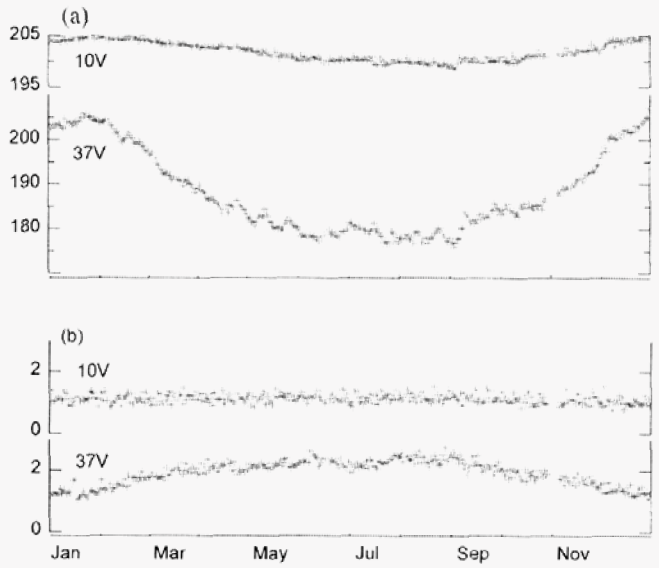

Fig. 5. Time series of AMSR-E *Tb* descending pass statistics for the year 2003 at Dome 'C', Antarctica, for 10 GHz and 37 GHz vertical polarizations: (a) Footprint mean, m_t; (b) Footprint standard deviation, σ_t. Units are in Kelvins.

of σ_m and $\overline{\sigma}$ in Figs. 4(b) and 4(c), respectively, indicate that there is a fairly large area centered at Salonga where $\overline{\sigma}$ and σ_m are very low, hence this area would be a good choice, considering homogeneity and stability, for an African tropical forest calibration site. For reference, Fig. 4(d) shows an image of the topography of the region at the EASE-Grid 25-km resolution.

C. *Antarctic*

A similar analysis to that for tropical forest was performed for the Antarctic ice sheet in a region around Dome Concordia (Dome C), centered at 75.0°S, 123.3°E. This site has meteorological instrumentation with long-term data records, and has been considered suitable as a long-wavelength (i.e., L-band) radiometer calibration site due to its dry climate and potentially stable emissivity characteristics [6], [14], [15].

Figs. 5(a) and 5(b) show the time series of m_t and σ_t at the location of Dome C. In comparison with the Salonga forest site the statistics at Dome C are influenced significantly by the annual cycle of the ice vertical temperature profile. The variation of the footprint *Tb* mean, m_t, shows a larger annual amplitude at 37 GHz, which samples near the surface, than at 10 GHz which samples deeper in the ice volume. The footprint *Tb* standard deviation, σ_t, is also larger at 37 GHz, peaking in the winter months, due to the lateral temperature gradients within the 3 x 3 footprint array, which are more pronounced near the surface.

Fig. 6 shows the images, similar to those of Fig. 4, of the *Tb* statistics for the Antarctic region around Dome C. The footprint *Tb* standard deviations, $\overline{\sigma}$, shown in Fig. 6(c) indicate a somewhat surprising amount of filamentary structure related to the features observed in Figs. 6(a) and (b), with standard deviations varying from less than 1 K to greater than 5 K over the distance of a few grid cells. These features indicate surface and/or subsurface spatial variability in the snow and ice temperature and/or emissivity structure giving rise to corresponding spatial variability in the brightness temperature. This spatial structure needs to be investigated further to be better understood. In both Fig. 4 and Fig.6 it is evident that the images of $\overline{\sigma}$ highlight 'edges' of features observed in the $\overline{m}$ and σ_m images. In terms of temporal variability over an annual cycle, the σ_m image in Fig. 6(b) indicates that the location of Dome C is not optimal; a location slightly to the southeast of Dome C would have significantly less temporal variability.

IV. Discussion

This paper has presented some examples, using time series and imagery of *Tb* spatial and temporal statistics, to investigate the suitability of ocean, forest and ice sheet sites for post-launch radiometric calibration. The stability of brightness temperatures averaged over the global ocean, and at carefully

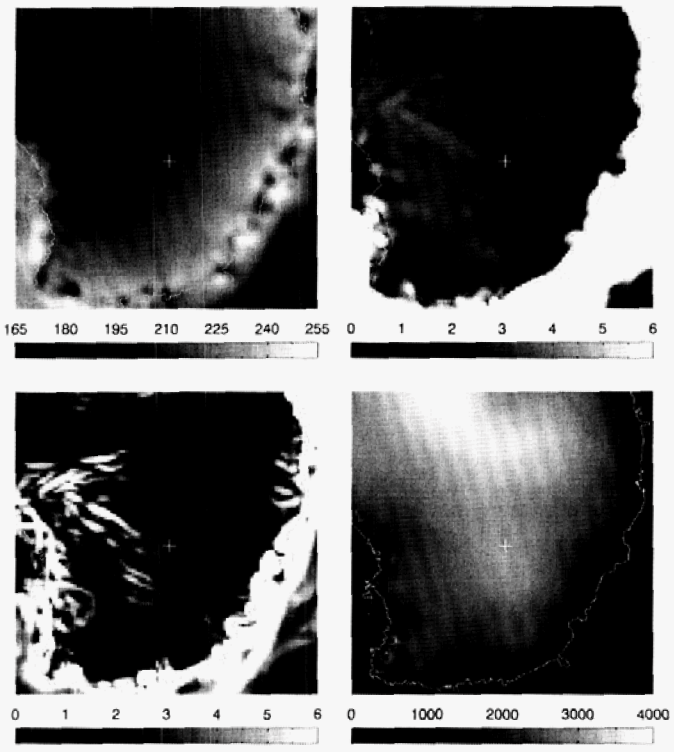

Fig. 6. Images of AMSR-E 10 GHz vertical polarization *Tb* statistics for southeast Antarctica, descending passes, in 2003. (a) *Upper left:* $\overline{m}$ (K). (b) *Upper right:* σ_m (K). (c) *Lower left:* $\overline{\sigma}$ (K). (d) *Lower right:* Surface topography (meters above sea level). [Note: Color scales are different in Figs. 4 and 6.]

selected forest sites, supports the use of these as stable calibration targets for the 6 to 37 GHz frequencies of SMMR, SSM/I, and AMSR-E, except for the 21.0/22.2/23.8 GHz and 85.5/89.0 GHz channels not considered here. This can be considered reasonable for land applications requiring calibration stability to within a few tenths Kelvin over a multi-year period, as indicated by the data in this paper, without the need to consider atmospheric effects. On the other hand, to intercalibrate data between sensors, it is necessary to consider absolute calibration in addition to calibration stability. For this purpose, radiative transfer modeling incorporating in-situ measurements of the surface and atmospheric characteristics is required, taking into account the specific frequencies, incidence angles, spatial resolutions and diurnal sampling of the sensors.

Our analysis of the Antarctic region has shown that there is significant spatial and temporal structure in the brightness temperatures at 6 to 37 GHz that limit the usefulness of the Dome C or other ice sheet area as a stable calibration target. However, it is clear that the ice sheet *Tb* variability decreases significantly at longer wavelengths, and hence ice sheets could prove useful calibration targets for radiometers operating at L-band.

ACKNOWLEDGMENTS

This work represents one phase of research carried out at the Jet Propulsion Laboratory, California Institute of Technology, and the CIRES National Snow and Ice Data Center, under contracts with the National Aeronautics and Space Administration.

REFERENCES

[1] H. Cosnefroy, M. Leroy, X. Briottet, "Selection and characterization of Saharan and Arabian desert sites for the calibration of opical satellite sensors,", *Remote Sens. Environ.*, vol. 58, pp. 101–114, 1996.

[2] M. Dinguirard and P. N. Slater, "Calibration of space-multispectral imaging sensrs: A review," *Remote Sens. Environ.*, vol. 68, pp. 194205, 1999.

[3] A. Bannari, K. Omari, P. M. Teillet, and G. Fedosejevs, "Potential of Getis statistics to characterize the radiometric uniformity and stability of test sites used for the calibration of Earth observation sensors," *IEEE Trans. Geosci. Rem. Sens.*, vol. 43, pp. 2918–2926.

[4] F. J. Wentz, "A well-calibrated ocean algorithm for special sensor microwave/imager," *J. Geophys. Res.*, vol. 102 no. C4, pp. 8703–8718, 1997.

[5] C. Ruf, "Detection of calibration drifts in spaceborne microwave radiometers using a vicarious cold reference," *IEEE Trans. Geosci. Rem. Sens.*, vol. 38, no. 1, pp. 44–52, 2000.

[6] A. Bingham and M. Drinkwater, "Recent changes in the microwave scattering properties of the Antarctic ice sheet," *IEEE Trans. Geosci. Rem. Sens.*, vol. 38, no. 4, pp. 1810–1820, 2000.

[7] S. T. Brown and C. S. Ruf, "Determination of an Amazon hot reference target for the on-orbit calibration of microwave radiometers," *J. Atmos. and Oceanic Tech.*, vol. 22. pp. 1340–1352, 2005.

[8] E. G. Njoku, S. K. Chan, W. Crosson, and A. Limaye, "Evaluation of the AMSR-E data calibration over land," *Rivista Italiana Di Telerilevamento (Italian Journal of Remote Sensing), 30/31*, 19–37 (in English), 2004.

[9] E. G. Njoku, B. Rague, and K. Fleming, "The Nimbus-7 SMMR pathfinder brightness temperature data set," *JPL Publication 98-4*, 56 pp., Jet Propulsion Laboratory, Pasadena, CA, 1998.

[10] K. Knowles, E. Njoku, R. Armstrong, and M. J. Brodzik, "Nimbus-7 SMMR Pathfinder daily EASE-Grid brightness temperatures, 1978-1987", National Snow and Ice Data Center, Boulder, CO, 2002.

[11] RSS, 1991

[12] R. L. Armstrong, K. W. Knowles, M. J. Brodzik, and M. A. Hardman, "DMSP SSM/I pathfinder daily EASE-Grid rightness temperatures, 1987-2005, National Snow and Ice Data Center, Boulder, CO, 1994, updated 2005.

[13] P. Ashcroft and F. Wentz, "Algorithm theoretical basis document (ATBD): AMSR Level 2A algorithm, *RSS Technical Report 121599-B1*, Remote Sensing Systems, Santa Rosa, 2000.

[14] E. Aristidi, K. Agabi, M. Azouit, E. Fossat, J. Vernin, T. Travouillon, et al., "An analysis of temperatures and wind speeds above Dome C, Antarctica," *Astronomy and Astrophysics*, vol. 430, pp. 739–746, 2005.

[15] V. Walden, M. Town, B. Halter, and J. Storey, "First measurements of the infrared sky brightness at Dome C, Antarctica," *Pub. Astr. Soc. Pacific*, vol. 117, pp. 300-308, 2005.